# Supporting Information

# Construction of planar-type defect-engineered metal-organic frameworks with both mixed-valence site and copper-ion vacancy for photocatalysis

Yuan Guo [a], Chao Feng [a], Shixin Wang [a], Yuehong Xie [a], Changyan Guo *[a], Ziran Liu [a], Naeem Akram [a], Yi Zhang [b], Yansong Zhao, [c] and Jide Wang *[a]

[a] Key Laboratory of Oil and Gas Fine Chemicals, College of Chemical Industry, Xinjiang University, Urumqi, 830046, China

[b] Hunan Provincial Key Laboratory of Chemical Power Sources, College of Chemistry and Chemical Engineering, Central South University, Changsha, 410083, China

[c] Department of Safety, Chemistry and Biomedical Laboratory Sciences, Faculty of Engineering and Science, Western Norway University of Applied Sciences, Inndalsveien28, 5063 Bergen, Norway

**Table of Content**

**SEM images for the screening of solvent type:**

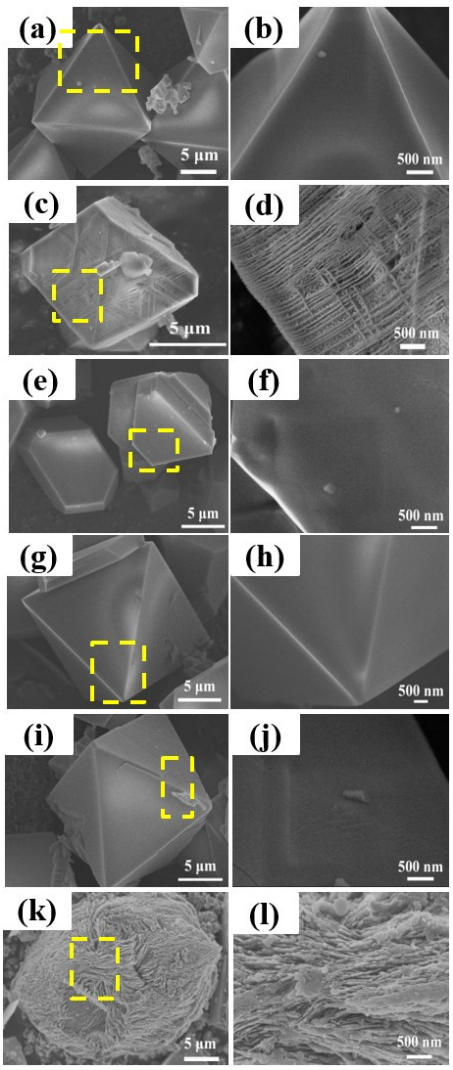


**Fig. S1.** SEM image for the HKUST-1 variants prepared with different solvents in the presence of 5 mM of VAN at 100°C for 12 h. (a),(b) MeOH; (c),(d) DMF:EtOH:$H_2O$ (1:1:1,v/v/v); (e),(f) EtOH:$H_2O$ (1:1,v/v); (g),(h) DMF:MeOH:$H_2O$ (1:1:1,v/v/v); (i),(j) DMF:$H_2O$ (1:1 ,v/v); (k),(l) MeOH:$H_2O$ (1:1 ,v/v).

The effects of different solvent types on the {111} face of HKUST-1 variants was studied in detail under concentration ratios of BTC, VAN and $Cu(NO_3)_2 \cdot 3H_2O$ was 1:4:2. No significant changes are observed on the {111} face of the crystal when the types of solvent were MeOH, DMF:EtOH:$H_2O$ (1:1:1,v/v/v), EtOH:$H_2O$ (1:1,v/v), DMF:MeOH:$H_2O$ (1:1:1,v/v/v) and DMF:$H_2O$ (1:1 ,v/v),

respectively (Fig. S1(a-b,e-j)). However, when the type of solvent was DMF:EtOH:$H_2O$ (1:1:1,v/v/v), NR-HKUST-1 with many nano-rods was synthesized, and those nano-rods were grown on nano-dots and distributed in parallel and interwoven with each other on the {111} face (Fig. S1(c-d)). In addition, when the type of solvent was MeOH:$H_2O$ (1:1 ,v/v), the crystal is broken and NS-HKUST-1 with nano-sheets was synthesized (Fig. S1(k-l)).

**SEM images for effect of vanillin concentration on HKUST-1:**

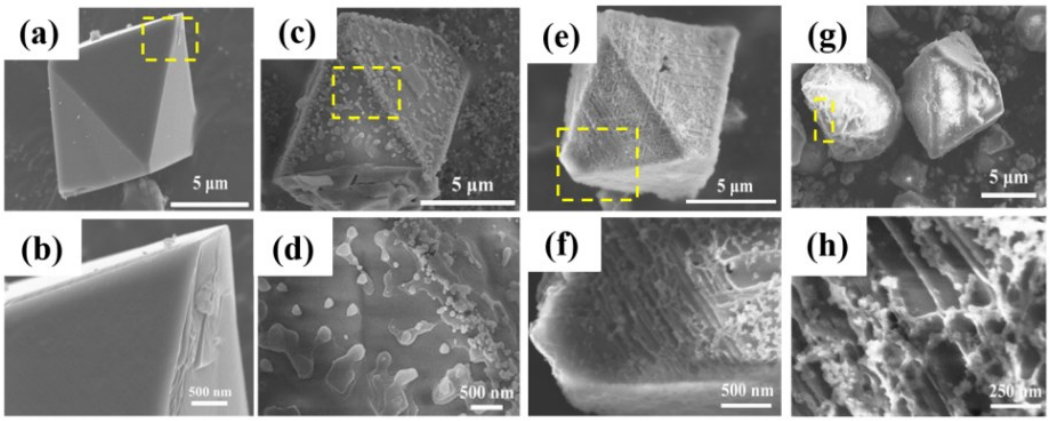


**Fig. S2.** SEM images of the HKUST-1 variants regulated by VAN obtained in DMF:EtOH:$H_2O$ (1:1:1, v/v/v) at 100°C for 12 h, and the variants prepared with different molar ratios of BTC and VAN. (a),(b) n(BTC):n(VAN)=3:1; (c),(d) 2:1; (e),(f) 1:4; (g),(h) 1:6.

The effects of different concentration ratios of VAN and BTC different on the {111} face of HKUST-1 was studied in detail under the conditions of $Cu(NO_3)_2 \cdot 3H_2O$ and BTC amounts was 3 mmol and 2 mmol, respectively. No significant changes are observed on the {111} face of the crystal at the concentration ratio of BTC and VAN was 3:1 (Fig. S2(a-b)). When the concentration ratio of BTC and VAN was 2:1, ND-HKUST-1 with uniformly dispersed nano-dots on the face of {111} was synthesized (Fig. S2(c-d)). When the concentration ratio of BTC and VAN was 1:4, many nano-rods

were grown on nano-dots, and these nano-rods were distributed in parallel and interwoven with each other on the {111} face of the crystal named NR-HKUST-1 (Fig. S2(e-f)). However, when the concentration ratio of BTC and VAN was 1:6, the crystal was broken and {111} face showed obvious groove (Fig. S2(g-h)).

**SEM images for effect of copper ion concentration on NR-HKUST-1:**

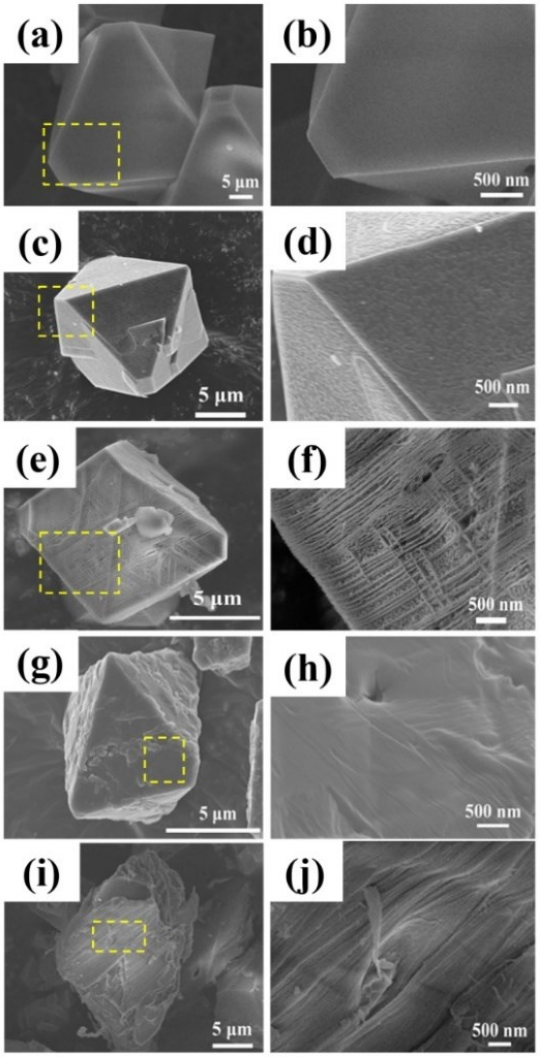


**Fig. S3.** SEM images of the HKUST-1 variants regulated by VAN obtained in DMF:EtOH:$H_2O$ (1:1:1, v/v/v) at 100°C for 12 h, and the variants prepared with different molar ratios of $Cu(NO_3)_2$•$3H_2O$ and BTC. (a).(b) n($Cu(NO_3)_2$•$3H_2O$ ):n(BTC)=1:2; (c).(d) 1:1; (e).(f) 2:1; (g).(h) 4:1; (i).(j) 5:1.

The effects of different concentration ratios of $Cu(NO_3)_2 \cdot 3H_2O$ and BTC on the {111} face of HKUST-1 variants was studied in detail under concentration ratios of BTC and VAN was 1:4. No significant changes are observed on the {111} face of the crystal at the concentration ratio of $Cu(NO_3)_2 \cdot 3H_2O$ and BTC was 1:2 (Fig. S3(a-b)). When the concentration ratio of $Cu(NO_3)_2 \cdot 3H_2O$ and BTC was 1:1, ND-HKUST-1 with nano-dots on the face of {111} was synthesized (Fig. S3(c-d)). When the concentration ratio of $Cu(NO_3)_2 \cdot 3H_2O$ and BTC was 2:1, NR-HKUST-1 with many nano-rods was synthesized, and those nano-rods were grown on nano-dots and distributed in parallel and interwoven with each other on the {111} face (Fig. S3(e-f)). However, when the concentration ratio of $Cu(NO_3)_2 \cdot 3H_2O$ and BTC was 4:1 or 5:1, the nano-dots and nano-rods on the surface disappear (Fig. S3(g-j)).

**SEM images for the effect of reaction temperature on NR-HKUST-1:**

The effects of different reaction temperature on the {111} face of NR-HKUST-1 was studied in detail under concentration ratios of BTC, VAN and $Cu(NO_3)_2 \cdot 3H_2O$ was 1:4:2. No significant changes are observed on the {111} face of the crystal when the reaction temperature was 80°C (Fig. S4 (a-b)). When the reaction temperature was 100°C, NR-HKUST-1 with many nano-rods was synthesized (Fig. S4(c-d)). However, when the reaction temperature was 150°C or 180°C, the crystal size decreases and the nano-rods disappear due to the rapid nucleation of the crystal (Fig. S4(e-h)).

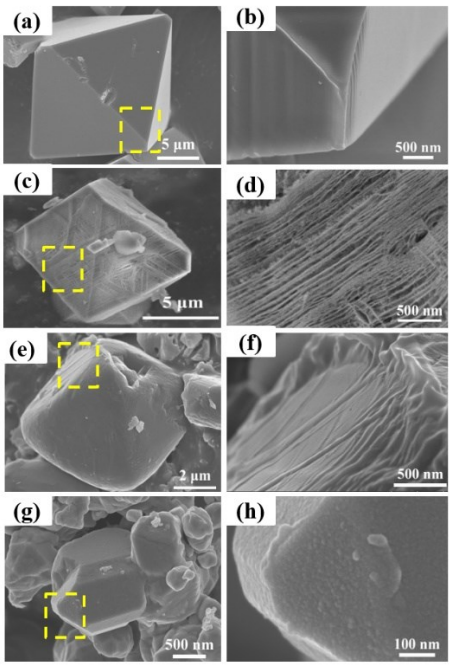


**Fig. S4.** SEM images for NR-HKUST-1 variants regulated by VAN obtained in DMF:EtOH:$H_2O$ (1:1:1, v/v/v) for 12 h at different reaction temperature. (a),(b) 80°C; (c),(d) 100°C; (e),(f) 150°C; (g),(h) 180°C.

**SEM images for the effect of reaction time on NR-HKUST-1:**

To explore the formation of nano-rods, the effects of different reaction time on the {111} face of NR-HKUST-1 were studied in detail under concentration ratios of BTC, VAN and $Cu(NO_3)_2 \cdot 3H_2O$ was 1:4:2. When the reaction time was 1 h, small particle of ND-HKUST-1 with uniformly dispersed nano-dots along the <100> direction on the face of {111} was synthesized (Fig. S5(a-b)). When the reaction time was 5 h, the nano-dots connections of the crystal along the <001> direction on the {111} face (Fig. S5(c-d)). When the reaction time was 12 h, NR-HKUST-1 with many dense nano-rods along the <011> and <101> direction on the {111} face was synthesized (Fig. S5(e-f)). However, when the reaction time was 33 h, the crystal with the bigger size was synthesized and these nano-rods along the <110> and <011> direction on the face of {111} tend to be smooth (Fig. S5(g-h)). When the NR-

HKUST-1 activated in the air for 10 days, NP-HKUST-1 with nano-plates growing in reverse direction on face {111} was synthesized, and these nano-plates penetrated into each other along the directions of <220> and <202> (Fig. S5(i-j)). The above results reveal that the process of formation of growing nano-rods into nano-rods and the inward growth process of nano-rods with the extension of reaction time due to the presence of vanillin.

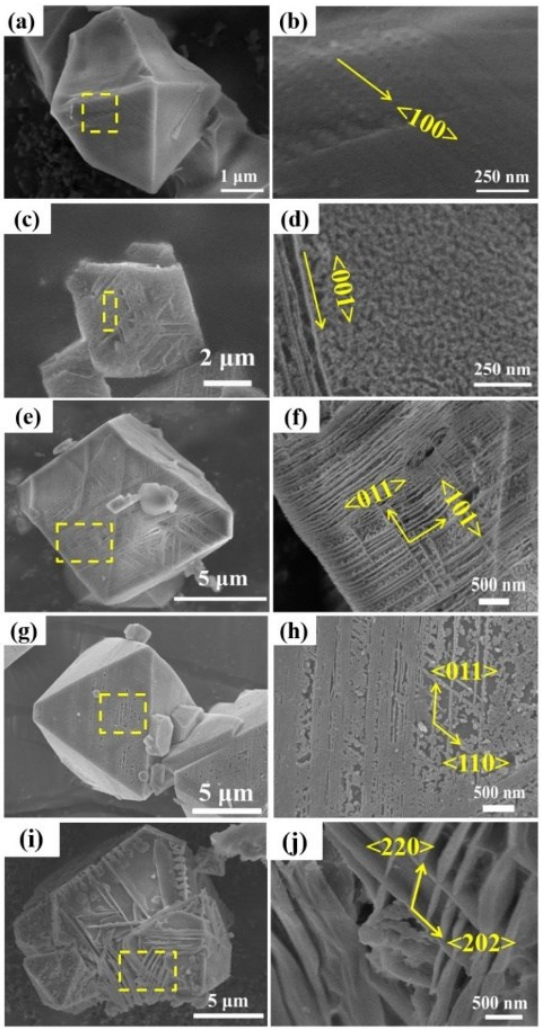


**Fig. S5.** SEM images for NR-HKUST-1 variants regulated by VAN obtained in DMF:EtOH:$H_2O$ (1:1:1, v/v/v) at 100°C prepared at different reaction time; (a),(b) 1 h; (c),(d) 5 h; (e),(f) 12 h; (g),(h) 33 h; (i),(j) activated in air for 10 days.

**SEM images for the effect of reaction temperature on NS-HKUST-1:**

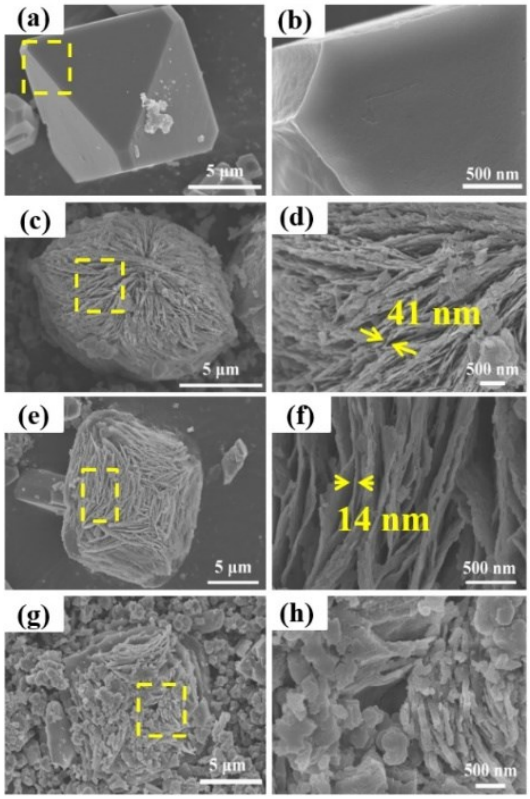


**Fig. S6.** SEM images for NS-HKUST-1 variants regulated by VAN respectively obtained in MeOH:$H_2O$ (1:1 (v/v)) for 12 h prepared at different reaction temperature. (a),(b) 80°C; (c),(d) 100°C; (e),(f) 150°C; (g),(h) 180°C.

The effects of different reaction temperature on the {111} face of NS-HKUST-1 variants was studied in detail under concentration ratios of BTC, VAN and $Cu(NO_3)_2 \cdot 3H_2O$ was 1:4:2. No significant changes are observed on the {111} face of the crystal when the reaction temperature was 80°C (Fig. S6(a-b)). When the reaction temperature was 100°C, NS-HKUST-1 with many nano-sheets was synthesized and the thickness of the nano-sheet was about 41 nm (Fig. S6(c-d)). When the reaction temperature was 150°C, the nano-sheet is about 14 nm (Fig. S6(e-f)). However, when the temperature continues to rise to 180°C, the crystals break up in large scale and the crystal size gets smaller due to the rapid nucleation of the crystal (Fig. S6(g-h)). The above results indicate that the nano-sheets thickness of NS-HKUST-1 can be controlled by appropriate reaction temperature.

**SEM images for the effect of reaction time on NS-HKUST-1:**

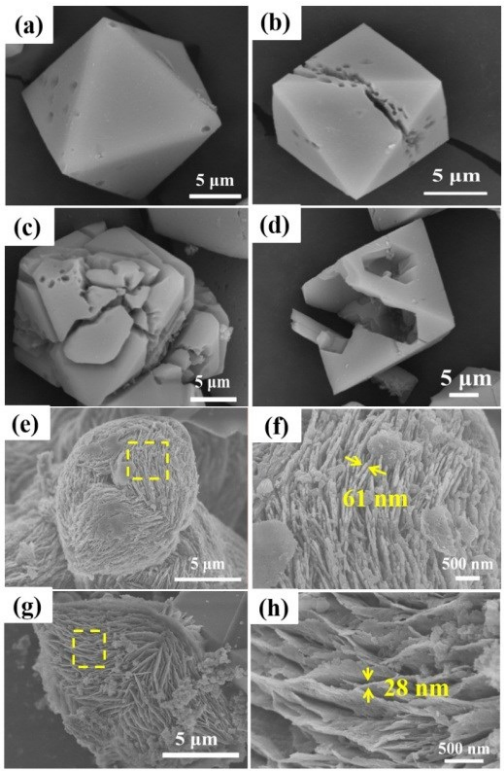


**Fig. S7.** SEM images for NS-HKUST-1 variants regulated by vanillin obtained in MeOH:$H_2O$ (1:1, v/v) at 150°C prepared at different time. (a) 3 h; (b) 5 h; (c-d) 7 h; (e-f) 10 h; (g-h) 33 h.

The effects of different reaction time on the {111} face of NS-HKUST-1 variants was studied in detail under concentration ratios of BTC, VAN and $Cu(NO_3)_2 \cdot 3H_2O$ was 1:4:2. When the reaction time was 3 h, NH-HKUST-1 with irregular distribution of nano-holes was synthesized (Fig. S7(a)). When the reaction time was 5 h and 7 h, the surface of crystal ruptured along the edge of the nano-holes (Fig. S7(b-d)). When the reaction time was 10 h, NS-HKUST-1 with nano-sheets was synthesized and the thickness of the nano-sheet was about 61 nm (Fig. S7(e-f)), larger than the 41nm synthesized at 12h (Fig. S6(c-d)). When the reaction time was 33 h, the thickness of the nano-sheet was about 28 nm (Fig. S7(g-h)). The above results indicate that the process of formation of the nano-

sheets on {111} face of NS-HKUST-1 with the increased reaction time and the nano-sheets thickness of NS-HKUST-1 can be controlled by appropriate reaction time.

**SEM images for activation and ultrasonic treatment on NR-HKUST-1 and NS-HKUST-1:**

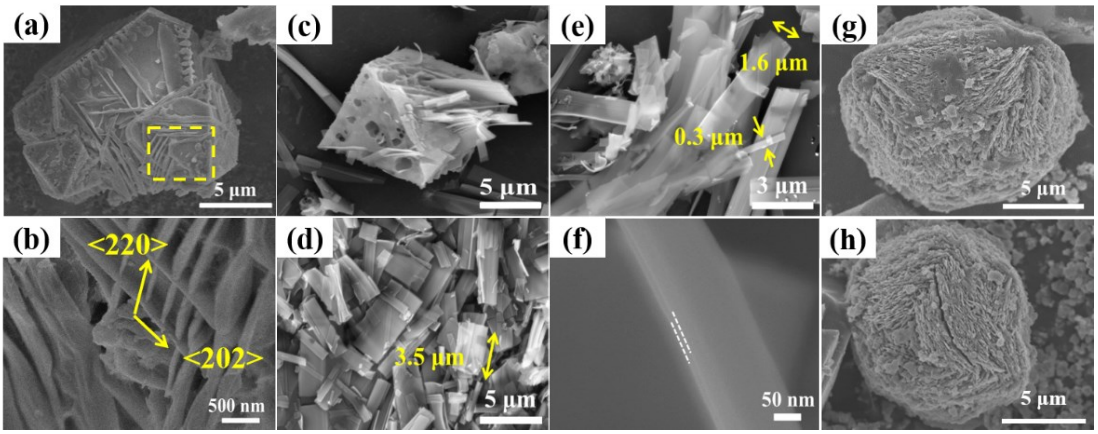


**Fig. S8.** SEM images in the process of activation and ultrasonic treatment of NR-HKUST-1: (a-b) activation for 10 days; (c) ultrasound for 10 min; (d-f) ultrasound 1 h; SEM images in the process of activation and ultrasonic treatment of NS-HKUST-1: (g) activation for 10 days; (d-f) ultrasound 2 h

Broken crystals and embedded nano-plates were found after ultrasonic treatment of NP-HKUST-1 for 10 min (Figu. S8(c)), which is further verified the phenomenon of reverse growth of nano-plates in it. When the ultrasound was continued for 1 h, the material was completely converted to a uniformly dispersed two-dimensional material 2D-HKUST-1 (Fig. S8(d-f)). This indicates that the bonding force between the nano-plates in NP-HKUST-1 is Van der Waals bond and can be destroyed by ultrasound.

**XRD, HRTEM images for the formation of 2D-HKUST-1:**

As shown in Fig. S9, 2D-HKUST-1 obtained after ultrasound belongs to the (220) facet of NP-HKUST-1 and HKUST-1. However, a weak peak of (400) and (600) facets was observed, which was attributed to the sample containing a very small amount of NP-HKUST-1 which had not been ultrasound into two-dimensional materials.

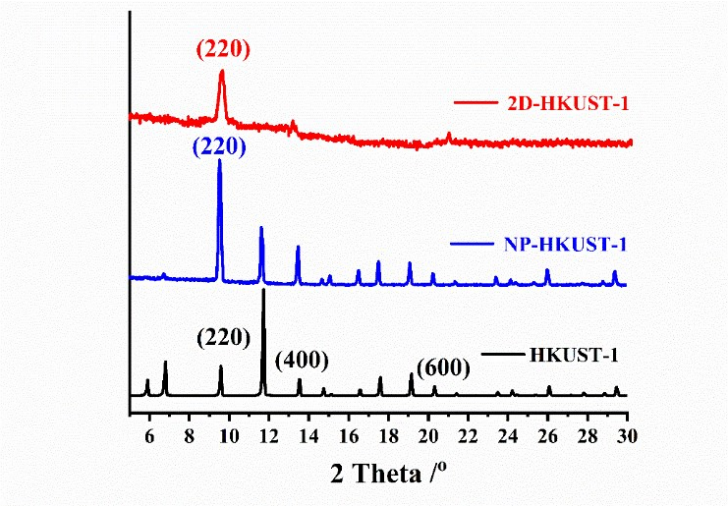


**Fig. S9.** Comparison of PXRD patterns of 2D-HKUST-1 with NP-HKUST-1 and parent HKUST-1.

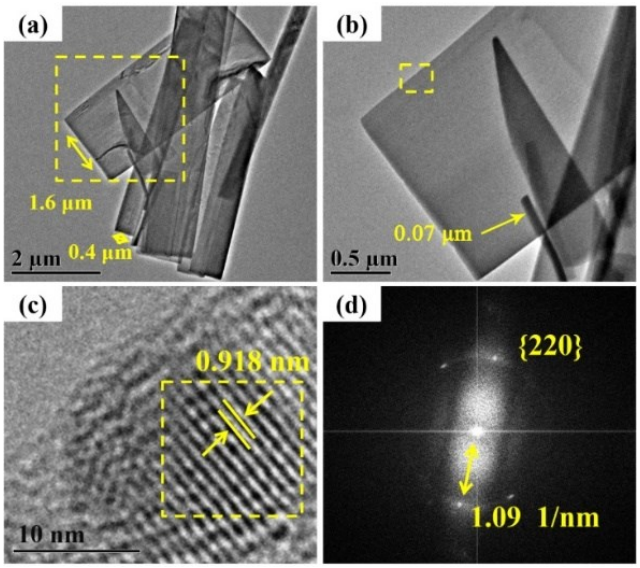


**Fig. S10.** TEM images (a-c) and HRTEM inverse FTT image (d) for 2D-HKUST-1.

The results are consistent with SEM (Fig. S8), TEM image revealed that the width of 2D-HKUST-1 was distributed between 0.07 - 1.6 μm (Fig. S10(a-b)).

**PXRD, HRTEM, SAED, FT-IR, Raman patterns of planar defect variants and parent HKUST-1:**

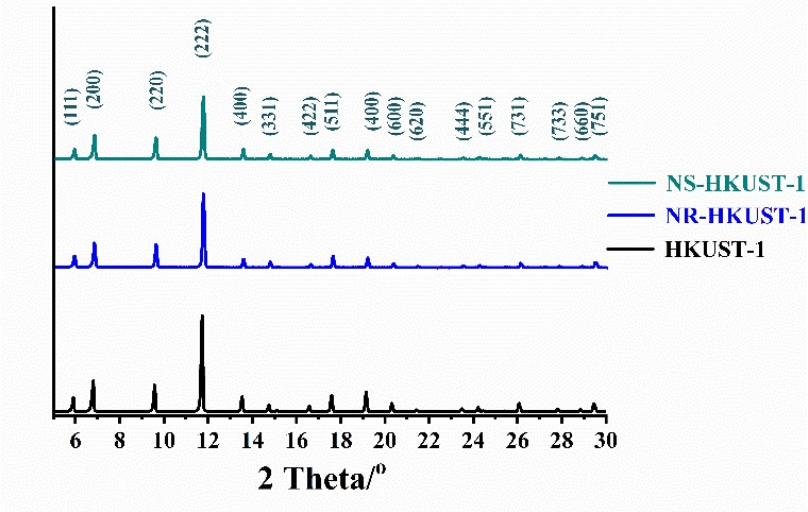


**Fig. S11.** Comparison of PXRD patterns of defective NR-HKUST-1 and NS-HKUST-1 with parent HKUST-1.

It can be seen from the XRD image that all diffraction peaks of HKUST-1 were consistent with reported literature (Fig. S11),[1] indicating that the parent HKUST-1 catalyst was successfully synthesized.

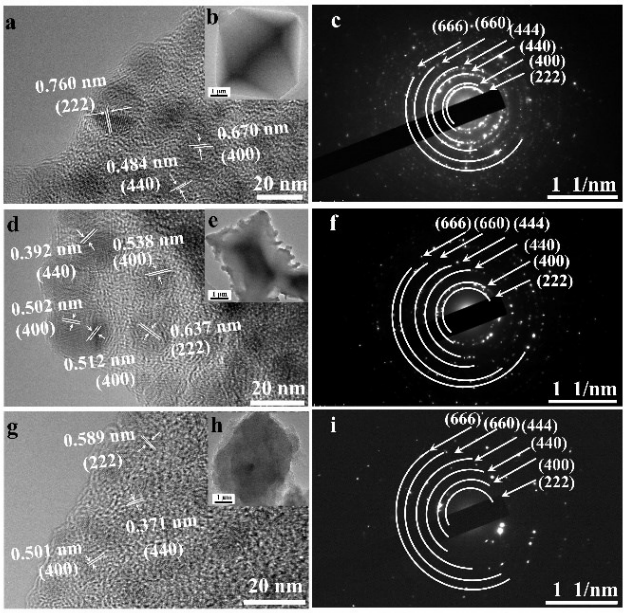


**Fig. S12.** HRTEM images of HKUST-1(a-b), NR-HKUST-1(d-e) and NS-HKUST-1(g-h), respectively. Selected area electron diffraction (SAED) images of HKUST-1(c), NR-HKUST-1(f) and NS-HKUST-1(i), respectively.

The HRTEM images of NR-HKUST-1 and NS-HKUST-1 were respectively shown in Fig. S12. The lattice spacing of NR-HKUST-1 was 0.637 nm, 0.538 nm and 0.392 nm, respectively, and that corresponding to its (222), (400) and (440) faces. The lattice spacing corresponding to (222), (400) and (440) faces of NS-HKUST-1 was measured to be 0.589 nm, 0.501 nm and 0.371 nm, respectively, which was generally respectively less than that of (222), (400) and (440) faces of parent HKUST-1 (0.760 nm, 0.670 nm and 0.484 nm). Moreover, SEAD images showed that the diffraction rings of parent could be well indexed into the (222), (400), (440), (444), (660) and (666) planes (Fig. S12(c)). However, the radius of diffraction rings of variants was smaller than that of the parent, suggesting that the lattice spacing could be reduced by introducting VAN, which is consistent with HRTEM analysis.

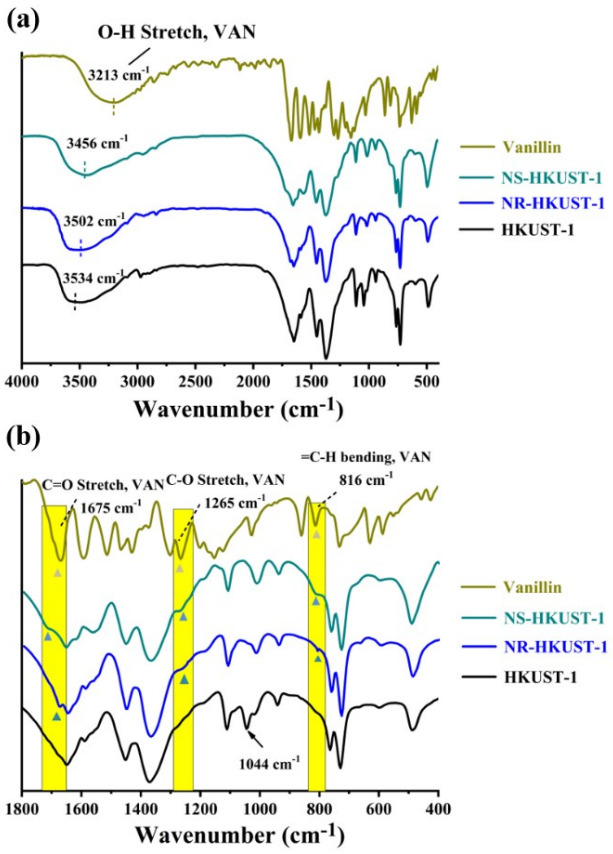


**Fig. S13.** Comparison of FT-IR spectra of defective NR-HKUST-1 and NS-HKUST-1 with parent HKUST-1 and vanillin.

The FT-IR spectra of HKUST-1 was consistent with the literature.[2] For HKUST-1, the acid C=O stretching vibration in the ligand BTC was shifted to 1653 $cm^{-1}$ after coordinating with $Cu^{2+}$. The Cu-O bond tensile vibration peak appeared at 725 $cm^{-1}$. The O-H stretching of carboxyl group appeared at 3100-3700 $cm^{-1}$ region. In addition, DMF in the partial solvents was adsorbed on the surface of HKUST-1, so a weak peak of C-N bond stretching vibration appeared at 1044 $cm^{-1}$.

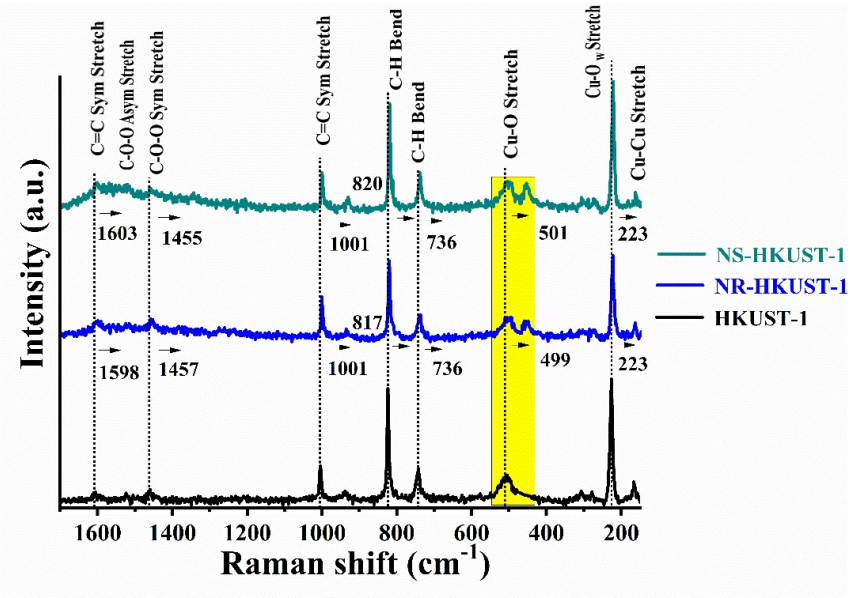


**Fig. S14.** Comparison of Raman spectra of defective NR-HKUST-1, and NS-HKUST-1 with parent HKUST-1.

As shown in Fig. S14, it can be seen that the Raman spectra of HKUST-1 was consistent with reports.[3] The Raman spectra of HKUST-1, NR-HKUST-1, and NS-HKUST-1 showed the same spectral characteristics. For HKUST-1, the C=C symmetric vibrational and stretching absorption peak on the benzene ring appeared at 1608 $cm^{-1}$ and 1004 $cm^{-1}$ respectively. The peak at 1525 $cm^{-1}$ and 1460 $cm^{-1}$ corresponds to the asymmetric and symmetric stretching of O-C-O respectively. The C-H out-of-plane bending of the corresponding benzene ring appeared at 823 $cm^{-1}$ and 745 $cm^{-1}$, respectively. The Cu-O stretching absorption peak of the carboxylate bridge appeared at 507 $cm^{-1}$. The doublet at 165 $cm^{-1}$ and the peak at 229 $cm^{-1}$ are assigned to a stretching mode involving Cu-Cu dimer and Cu-$O_w$ respectively, where $O_w$ indicates the oxygen of the water molecule adsorbed on $Cu^{2+}$ ion.

**$^{1}$H-NMR and $^{13}$C-NMR spectra, HPLC and EA-CHNS analysis of catalysts:**

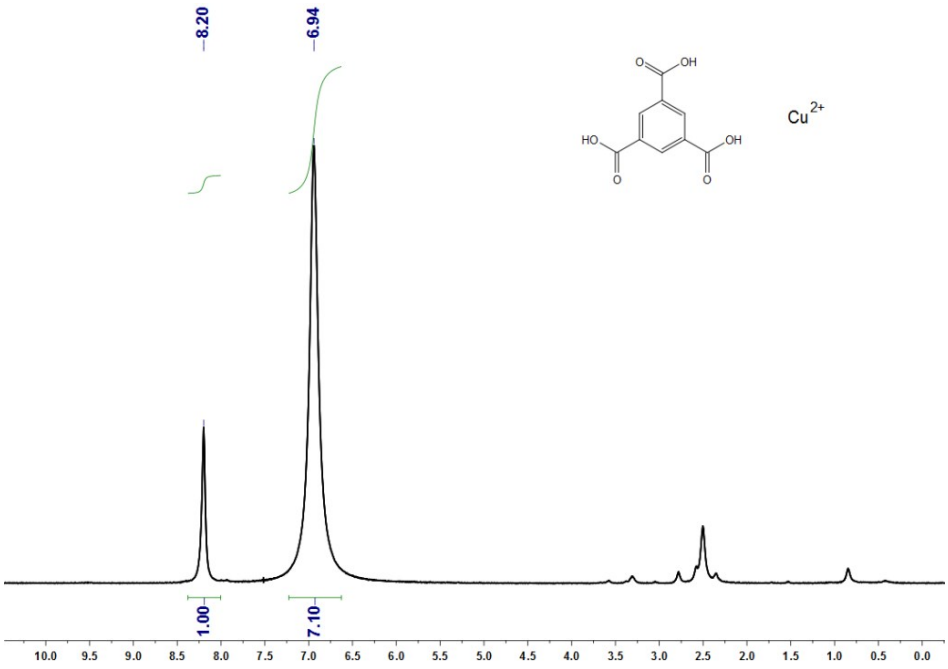


**Fig. S15.** $^{1}$H-NMR spectra analysis of the dissolved HKUST-1. ($^{1}$H NMR (400 MHz, DMSO) δ 8.20 (s, 1H), 6.94 (s, 7H)).

According to literature reports,[4] the organic ligand coordinated with copper ions in the dissolved samples, which leads to a great change in the chemical environment of the proton, accompanied by a great shift in the chemical shift. The integration for the hydrogen atoms in carboxyl (δ=8.20) from BTC was set as 1. The integration for the hydrogen atoms in benzene ring (δ=6.94) from BTC was 7. The peak δ<4.0 was considered to be solvent deuterium DMSO, DCl and a small amount of impurity. Theoretically, hydrogen atoms of carboxyl and benzene ring should be 1:1, but carboxyl group needs to be deprotonized to coordinate with copper ion in HKUST-1. Therefore, for the synthesis of HKUST-1 in this experiment, on average, 6 carboxyl groups coordinate with copper ions in every 2.3 BTC molecule (7/3).

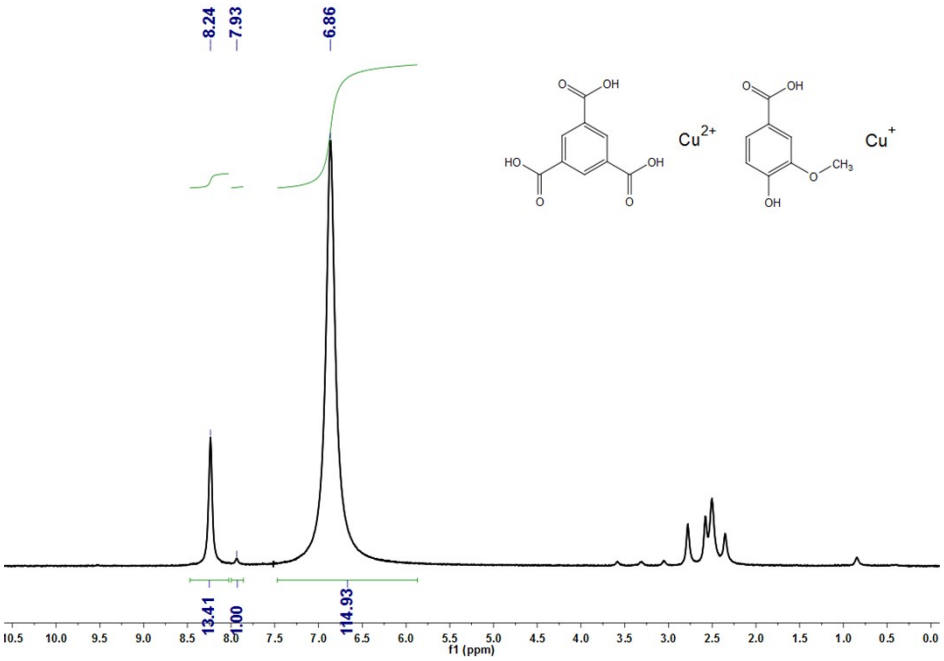


**Fig. S16.** $^{1}$H-NMR spectra analysis of the dissolved NR-HKUST-1. ($^{1}$H NMR (400 MHz, DMSO) δ 8.24 (s, 13H), 7.93 (s, 1H), 6.86 (s, 115H)).

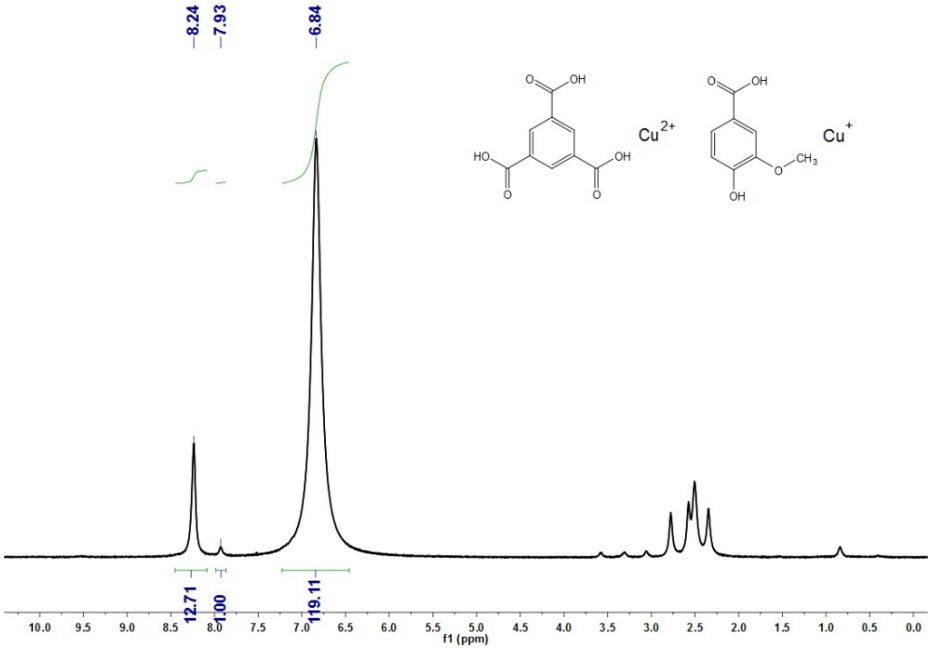


**Fig. S17.** $^{1}$H-NMR spectra analysis of the dissolved NS-HKUST-1. ($^{1}$H NMR (400 MHz, DMSO) δ 8.24 (s, 13H), 7.93 (s, 1H), 6.84 (s, 119H)).

For NR-HKUST-1, the integration for the hydrogen atoms in -OH (δ=7.93) from vanillic acid

was set as 1. The integration for the hydrogen atoms in benzene ring (δ=6.86) from BTC and vanillic acid was 115. The integration for the hydrogen atoms in COOH (δ=8.24) from BTC and vanillic acid was 13. The chemical shift of $CH_3$- group in vanillic acid at 2.0~3.0 range, which are not easy to be studied in detail because δ<4.0 contains interference of solvent peaks.

For NS-HKUST-1, because δ<4.0 contains solvent peak, the $CH_3$- group in vanillic acid are not easy to be studied in detail. The integration for the hydrogen atoms in -OH (δ=7.93) from vanillic acid was set as 1. The integration for the hydrogen atoms in carboxyl (δ=8.24) from BTC and vanillic acid was 13. The integration for the hydrogen atoms in benzene ring (δ=6.84) from BTC and vanillic acid was 119.

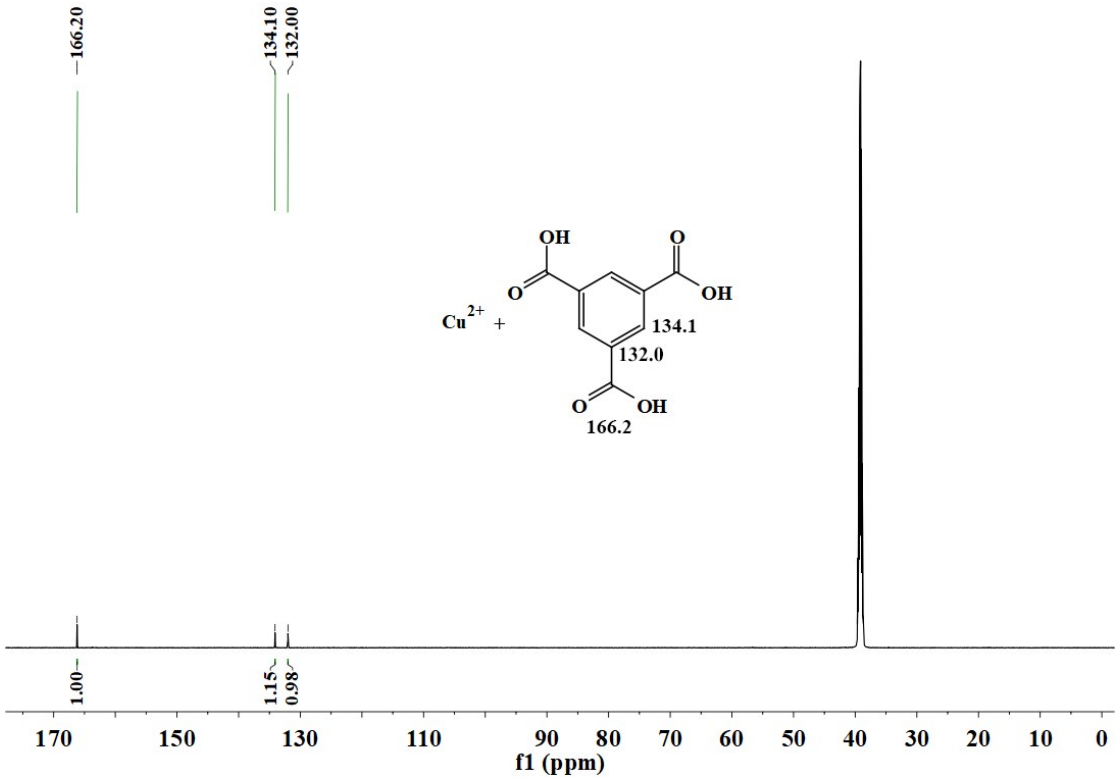


**Fig. S18.** $^{13}$C-NMR spectra analysis of the dissolved HKUST-1.

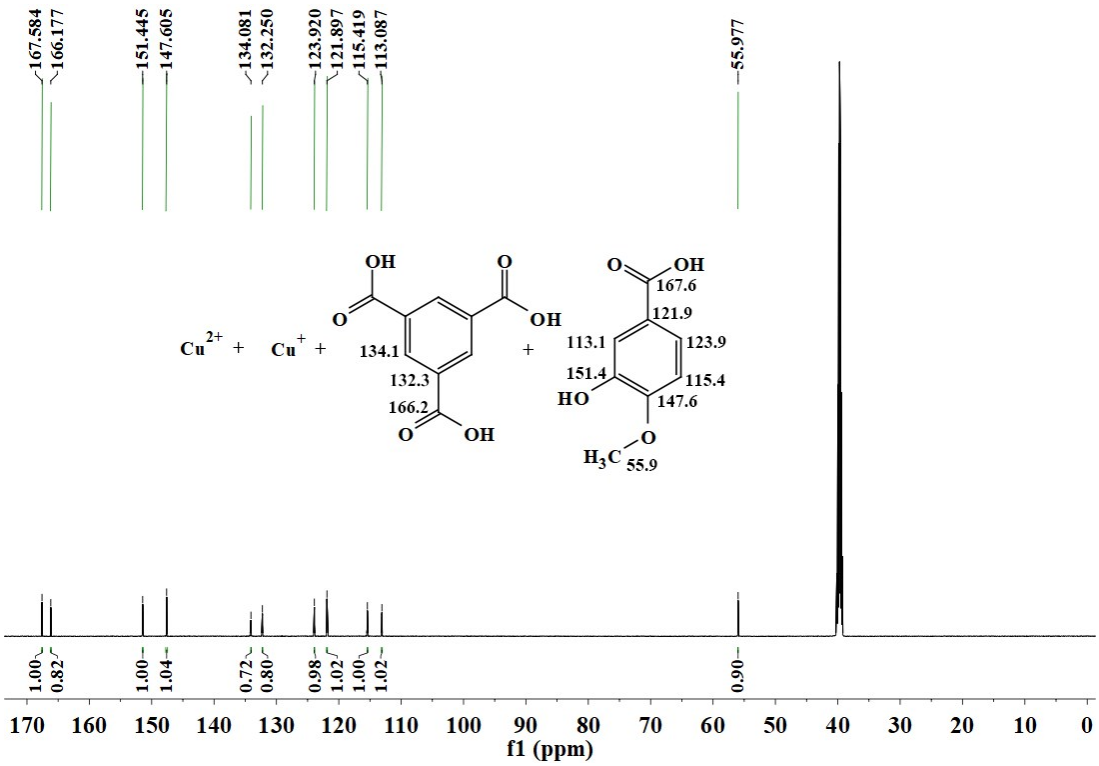


**Fig. S19.** $^{13}$C-NMR spectra analysis of the dissolved NR-HKUST-1.

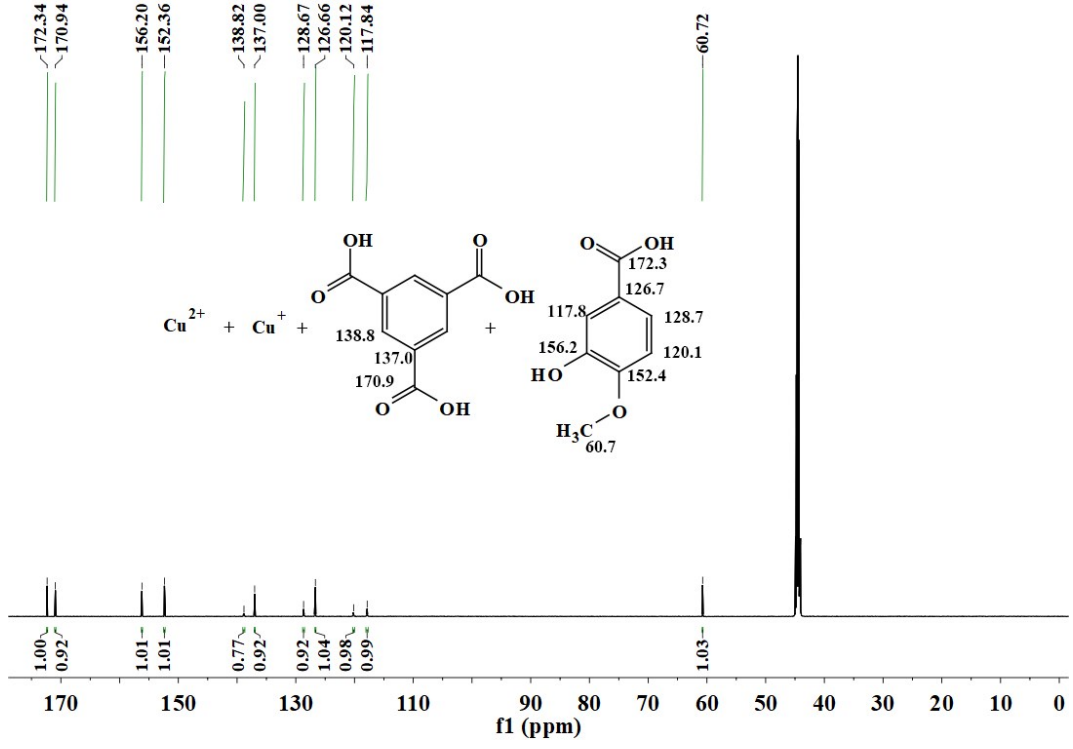


**Fig. S20.** $^{13}$C-NMR spectra analysis of the dissolved NS-HKUST-1.

In all $^{13}$C-NMR spectra the BTC linker is represented by peaks at ~132, ~134 and ~166 ppm for different carbon atoms respectively, and the peaks at ~40 ppm is solvent deuterium DMSO (Fig. S18-S20). The $^{13}$C-NMR spectra of NR-HUKST-1 and NS-HKUST-1 further confirm the co-existence of BTC and vanillic acid (Fig. S19-S20), and the vanillic acid linker can be confirmed by the new peaks located at ~56, ~113, ~115, ~122, ~124, ~147, ~145 and ~167 ppm compared with parent HKUST-1. While, the shift of peak in the $^{13}$C-NMR spectra of NR-HUKST-1 and NS-HKUST-1 may be caused by coordination with copper ions. In addition, the carbon (HC=CH) atoms peak area ratio of BTC (134.0 ppm) and vanillic acid (113.0 ppm) in NR-HUKST-1 is 0.72 : 1.02, among which there are three carbon (HC=CH) atoms in BTC and one in vanillic acid, revealing that the ratio between BTC and VAN molecules is 1:4. In NS-HUKST-1, the carbon (HC=CH) atoms peak area ratio of BTC (138.8 ppm) and vanillic acid (117.8 ppm) in NR-HUKST-1 is 0.77 : 0.99, which is also revealed that the ratio between BTC and VAN molecules is 1:4.

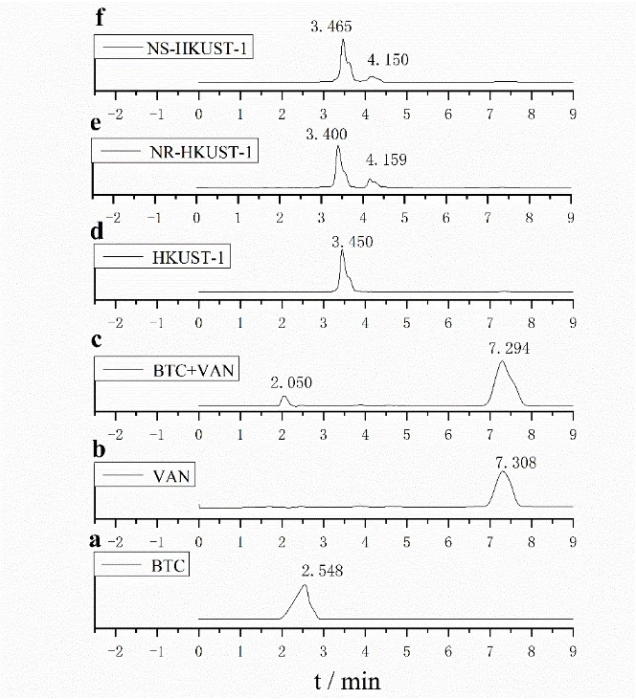


**Fig. S21.** HPLC analysis of the dissolved HKUST-1, NR-HKUST-1, and NS-HKUST-1.

In this separation system, the retention time of BTC and VAN was 2.504 min and 7.308 min, respectively (Fig. S21(a,b)), which was consistent with the retention time in the separation of BTC and VAN mixtures (Fig. S21(c)). However, in HKUST-1, the retention time of BTC – $Cu^{2+}$ bound intermediate moved to 3.450 min (Fig. S21(d)). In NR-HKUST-1 and NS-HKUST-1, VAN – $Cu^{1+}$ bound intermediate moved to 4.155 min, and the intermediate ratio of BTC and VAN was calculated as 1:4 (Fig. S21(e-f)).

**Table S1** The EA-CHNS analysis of HKUST-1, NR-HKUST-1, and NS-HKUST-1.

| Element (%) | HKUST-1 | NR-HKUST-1 | NS-HKUST-1 |
|---|---|---|---|
| C | 36.73 | 31.35 | 31.52 |
| H | 12.09 | 22.31 | 22.28 |

It is assumed that there are five organic linkers in HKUST-1 and NR-HKUST-1 respectively, among which, the 5 organic linkers in HKUST-1 are all BTC molecule, while the 5 organic linkers in NR-HKUST-1 are one BTC molecule and four VAN molecules. And H atoms on -COOH and -OH group are removed due to deprotonation during coordination with copper ion. Next, it is calculated that the ratio of $C_{HKUST-1}$:$H_{HKUST-1}$ is 3:1, while the ratio of $H_{HKUST-1}$:$H_{NR-HKUST-1}$ and $C_{HKUST-1}$:$C_{NR-HKUST-1}$ is 1:1.8 and 1.17:1, respectively, which is completely consistent with the EA-CHNS analysis, and confirm that the ratio (BTC: vanillic acid) is 1:4.

**UV-vis absorption spectra for competitive coordination of VAN and BTC:**

As shown in Fig. S22, the competitive coordination relationship between VAN and BTC was monitored by UV-Vis absorption spectra. The absorption peak of the $Cu(NO_3)_2 \cdot 3H_2O$ solution (blue) appears at 253 nm (Fig. S22(a)). The absorption peak of the VAN solution (colorless) appeared at 279 nm and 312 nm (Fig. S22(b)). The absorption peak of the BTC solution (colorless) appeared at 247

and 302 nm (c). After adding VAN to $Cu(NO_3)_2$•$3H_2O$ solution, the absorption peaks of the mixed solution were red-shifted and blue-shifted to 280 nm and 309 nm, respectively, and the color of the solution quickly turned green (Fig. S22(b)). When the BTC solution was slowly added to the mixed solution of VAN and Cu(II), the absorption peak at 280 nm formed by the coordination effect of VAN and Cu(II) was blue-shifted to 279 nm.

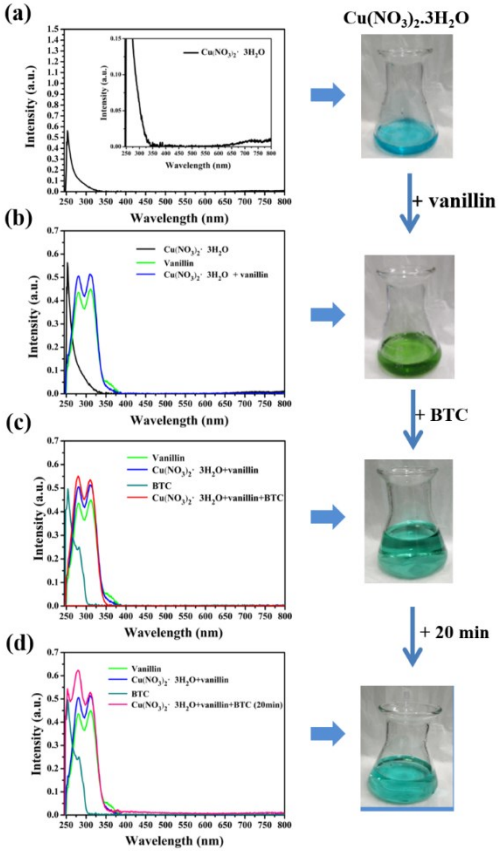


**Fig. S22.** UV-vis absorption spectra of different sample solutions. (a): $Cu(NO_3)_2$•$3H_2O$; (b): Vanillin was added dropwise to the solution (a); (c): BTC was added dropwise into solution (b); (d): solution (c) was stirred for 20 min at room temperature.

Meanwhile, the intensity of the peaks at 279 nm and 309 nm increased rapidly and the color of the solution gradually changed from green to blue-green (Fig. S22(c)), indicating that BTC could destroy

the coordination of VAN and Cu(II). After stirring at room temperature for 20 min, it was found that the coordination absorption peak of Cu(II) and VAN did not completely disappear (Fig. S22(d)). However, the absorption peak at 309 nm was red-shifted to 311 nm and the coordination absorption peak of BTC and Cu(II) appeared at 253 nm, and the color of the solution became bluer. The above experimental results show that BTC and VAN have competitive coordination in the synthesizing process of defective HKUST-1. Due to the stronger coordination ability of BTC, it can rapidly coordinate with Cu ions, thereby destroying the coordination between Cu (II) and VAN. However, the coordination between Cu(II) and VAN is not completely destroyed, resulting in obvious defects on the crystal surface at the later stage of crystal formation.

**Scheme of planar-type defective NR-HKUST-1 and NS-HKUST-1 in different growth:**

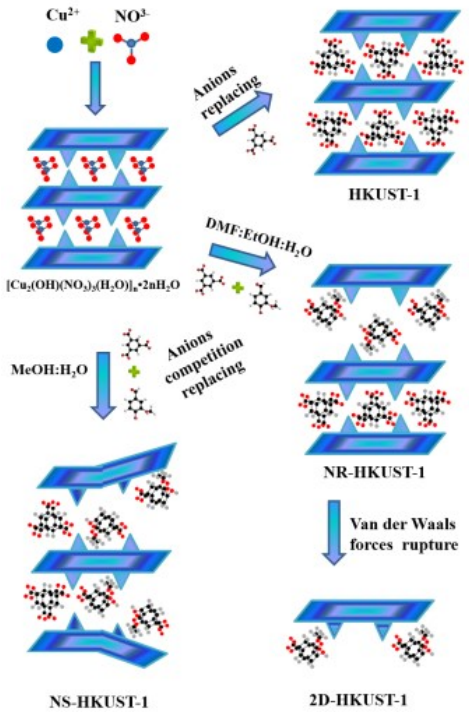


**Fig. S23.** Schematic drawing of a proposed formation mechanism of planar defects and 2D-HKUST-1 by regulation of vanillin.

**EPR, $N_2$ BET and TGA analysis of planar defect variants and parent HKUST-1:**

As shown in Fig. S24, EPR test revealed that HKUST-1 has a certain concentration of copper ion vacancy because of an inevitable defect in the process of synthesis, and the g value is 2.14, which is consistent with the literature report. [4] However, the copper vacancy defect concentrations of NR-HKUST-1, and NS-HKUST-1 regulated by VAN were all higher than HKUST-1. The copper ion vacancy defect concentration of NR-HKUST-1 in the <110> and <111> direction was higher than and HKUST-1. NS-HKUST-1 has obvious copper ion vacancy defect concentration in the direction of <111>, <100> and <110>. This result is in good agreement with the analysis of SEM test (Fig. S6-S7). It also can be justified that NS-HKUST-1 had the widest g value peak, which indicates that it had the most delocalized electron.

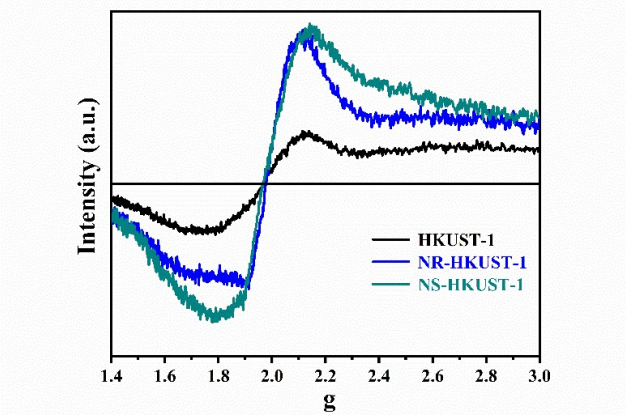


**Fig. S24.** Comparison of EPR patterns of copper ion vacancy of defective NR-HKUST-1, and NS-HKUST-1 with parent HKUST-1.

The $N_2$ adsorption/desorption isotherms of HKUAT-1 and planar defect variants were type I according to the IUPAC classification of isotherm shapes (Fig. S24(a)), and parent HKUST-1 reflect pore size distributions in micropore with peak distributions at 0.5 nm (Fig. S24(b)), which result is in good agreement with the literature. [6] The specific surface area and total pore volume of HKUST-1 was

1267 $m^2/g$ and 0.5019 $cm^3/g$ respectively (Table S2), which were lower compared to the literature due to differences in the activation process.

**Table S2** BET surface areas and pore features of hierarchical porous HKUST-1, NR-HKUST-1, and NS-HKUST-1.

| Sample | $S_{BET}$[a] | Pore volumes ($cm^3/g$) | | |
|---|---|---|---|---|
| | ($m^2/g$) | $V_{total}$[b] | $V_{micro}$[c] | $V_{meso}$[d] |
| HKUST-1 | 1267 | 0.5019 | 0.4748 | 0.0255 |
| NR-HKUST-1 | 1484 | 0.6611 | 0.5644 | 0.1000 |
| NS-HKUST-1 | 883 | 0.3580 | 0.3333 | 0.0268 |

[a] **SBET**: Brunauer–Emmett–Teller (BET) surface area. [b] **Vtotal**: Total pore volume calculated from the nitrogen adsorption data at $P/P_0 = 0.998$. [c] **Vmicro**: Micropore volume obtained by the t-plot method. [d] **Vmeso**: Mesopore volume calculated by the Barrett–Joyner–Halenda (BJH) adsorption method.

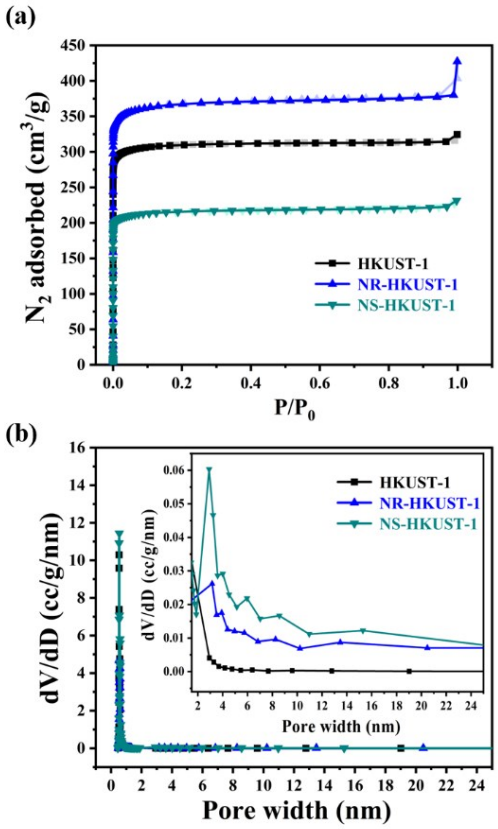


**Fig. S25.** Comparison of the $N_2$ adsorption/desorption isotherms (a) and pore size distribution curves (b) at 77 K of defective NR-HKUST-1 and NS-HKUST-1with parent HKUST-1.

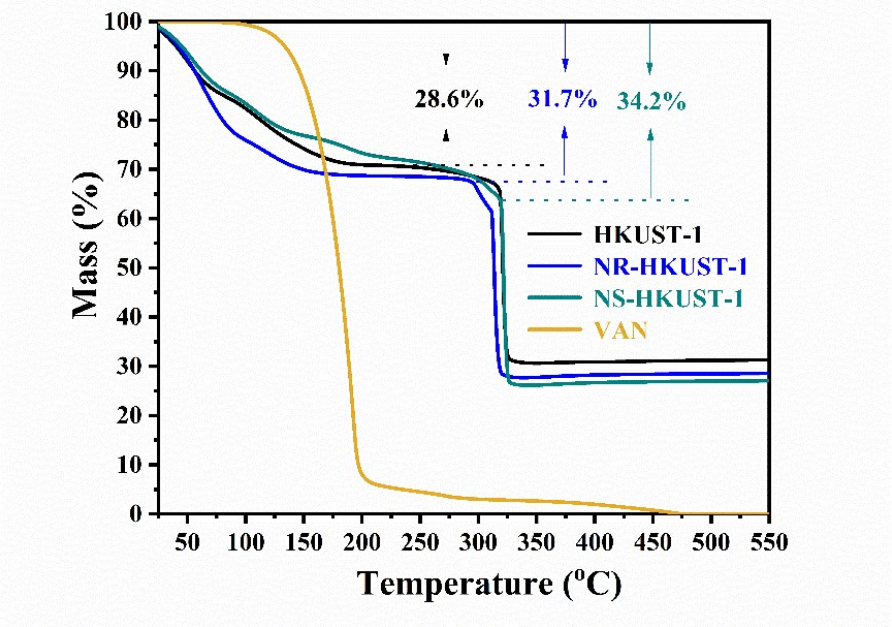


**Fig. S26.** Comparison of TGA images of defective NR-HKUST-1, and NS-HKUST-1 with parent HKUST-1.

### XPS and AES spectroscopic analysis of planar defect variants and parent HKUST-1:

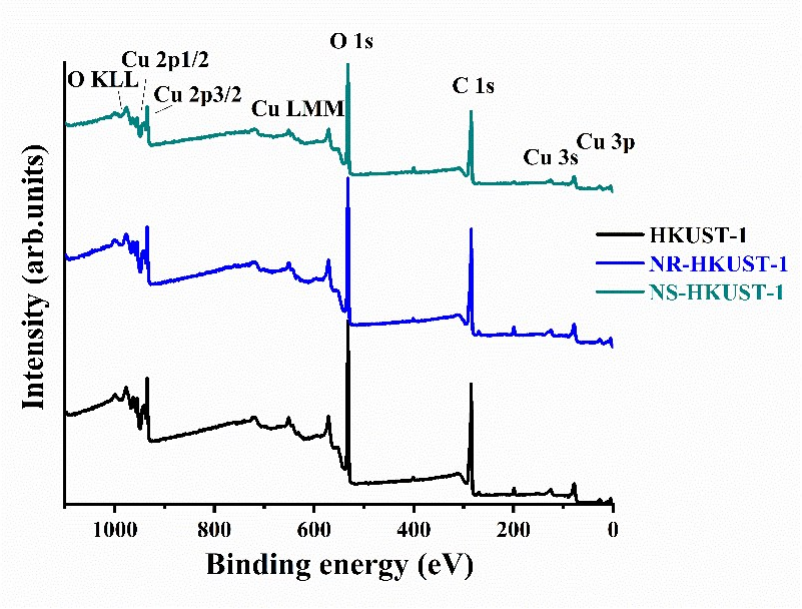


**Fig. S27.** XPS survey scans for HKUST-1, NR-HKUST-1, and NS-HKUST-1.

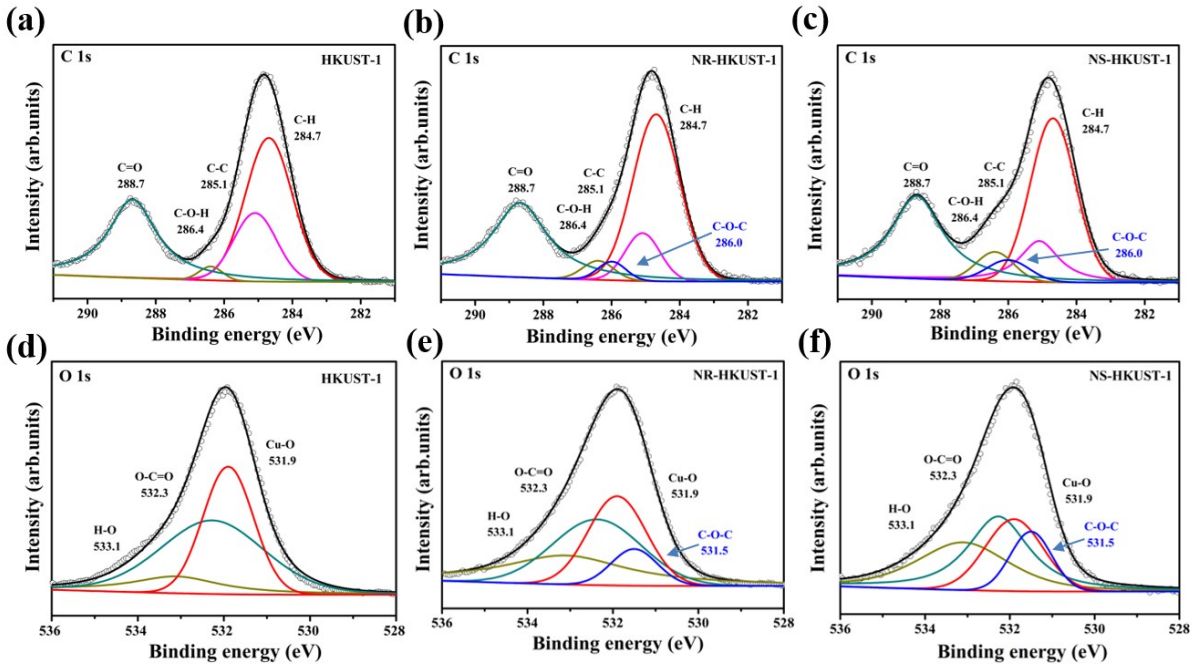


**Fig. S28.** Deconvoluted C 1s (a, b, c) and O 1s (d, e, f) peaks for the samples: HKUST-1, NR-HKUST-1, and NS-HKUST-1.

As shown in Fig. S28, For C 1s and O 1s, HKUST-1 showed peaks corresponding to C=O, C-O-H, C-C and C-H at binding energies of 288.7 eV, 286.4 eV, 285.1 eV and 284.7 eV, respectively. In addition, peaks corresponding to H-O, O-C=O, and Cu-O appeared at the binding energies of 533.1 eV, 532.3 eV and 531.9 eV respectively, which were consistent with the literature. [7] But for NR-HKUST-1 and NS-HKUST-1, the peaks of C 1s and O 1s from C-O-C appear at 286.0 eV and 531.5 eV respectively. These results show that in the process of competitive coordination between VAN and BTC, VAN successfully coordinates with copper ions.

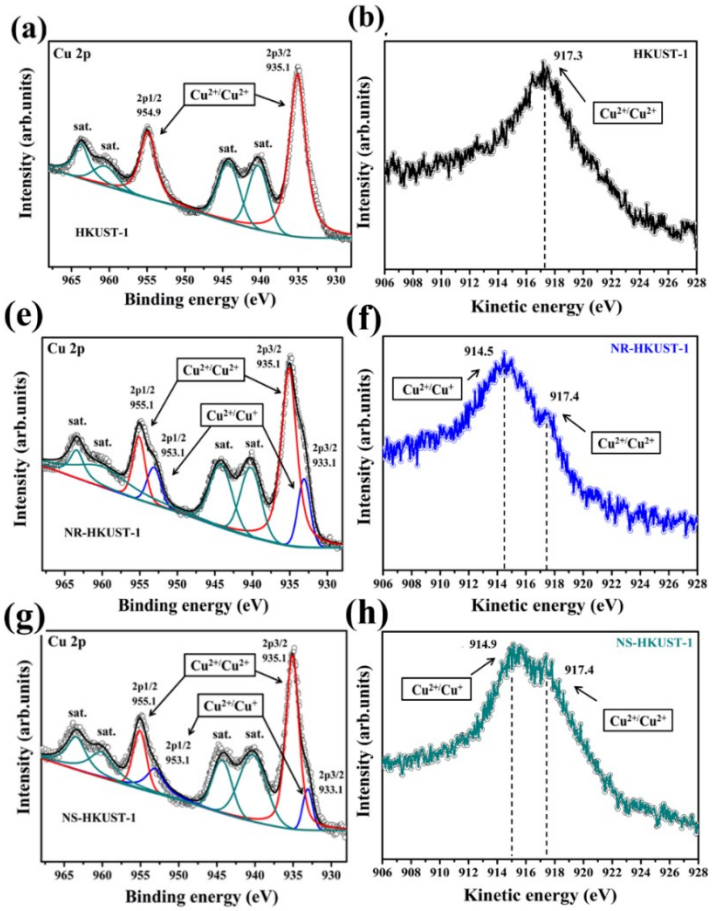


**Fig. S29.** Deconvoluted Cu 2p peaks (a, c, e) and Auger spectra (b, d, f) for the samples: HKUST-1, NR-HKUST-1, and NS-HKUST-1.

As shown in Fig. S29, For Cu 2p, the binding energy of 935.1 eV and 955.1 eV, which were attributed to the characteristic peaks of Cu $2p_{3/2}$ and Cu $2p_{1/2}$ respectively, and the binding energy of 940.3-944.2 eV and 960.5-963.7 eV were the satellite peaks, indicating that all the samples exist in the form of $Cu^{2+}/Cu^{2+}$ dimer and occupies the dominant part. The Cu component in parent HKUST-1 only has the form of $Cu^{2+}/Cu^{2+}$ dimer, which is similar to the literature report.[8] However, for NR-HKUST-1 and NS-HKUST-1, $Cu^{1+}/Cu^{2+}$ dimer appeared at binding energies of 933.1 eV and 953.1 eV. The presence of two kinds of dimers for NR-HKUST-1 and NS-HKUST-1 is further supported by the Auger peaks at ~914.5 eV for $Cu^{1+}/Cu^{2+}$ and at ~917.3 eV as a shoulder for $Cu^{2+}/Cu^{2+}$ species.

## XPS analysis of HKUST-1 variants regulating by other aldehydes and carboxylic acids:

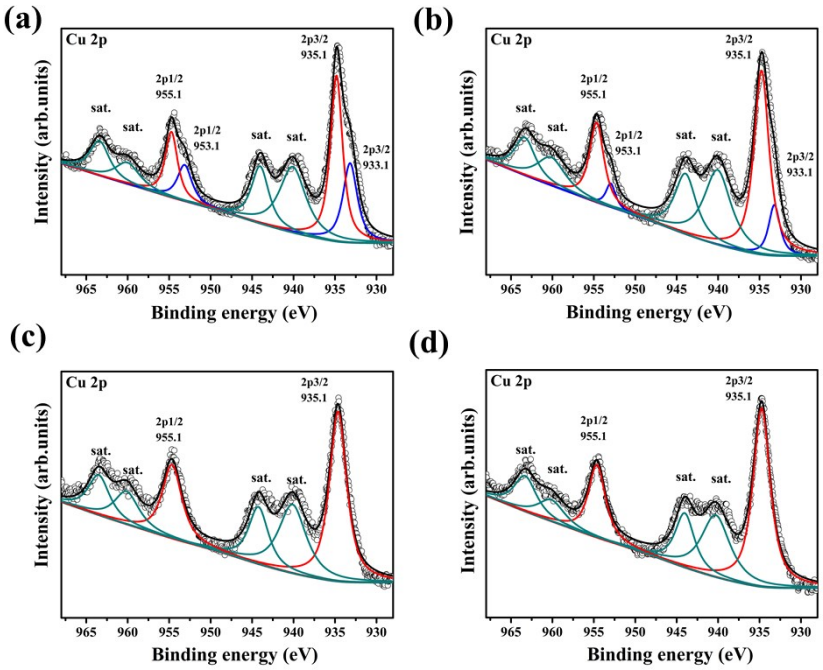


**Fig. S30.** Deconvoluted Cu 2p peaks for the HKUST-1 variants regulating by formaldehyde(a), benzaldehyde(b), formic acid(c) and benzoic acid(d), respectively.

## The SBU of HKUST-1 and defective HKUST-1:

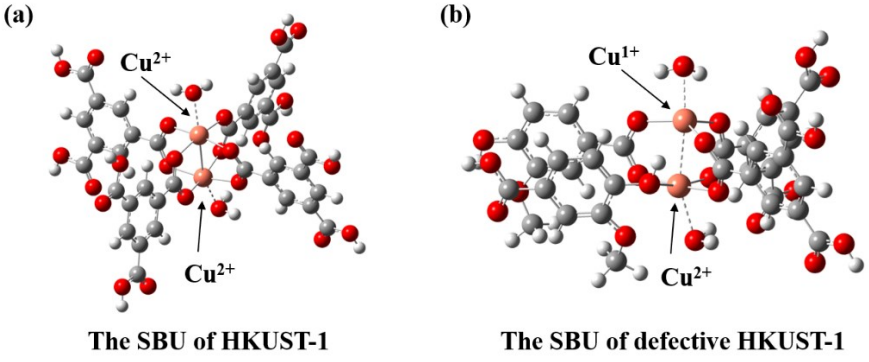


**Fig. 31.** (a) The structure of a Cu−Cu paddlewheel unit from HKUST-1. (b) The structure of a Cu−Cu paddlewheel unit from NR-HKUST-1 and NS-HKUST-1. (color code of the atoms: Cu, brown; C, gray or black; O, red; H, white).

## FWHM patterns of planar defect variants and parent HKUST-1:

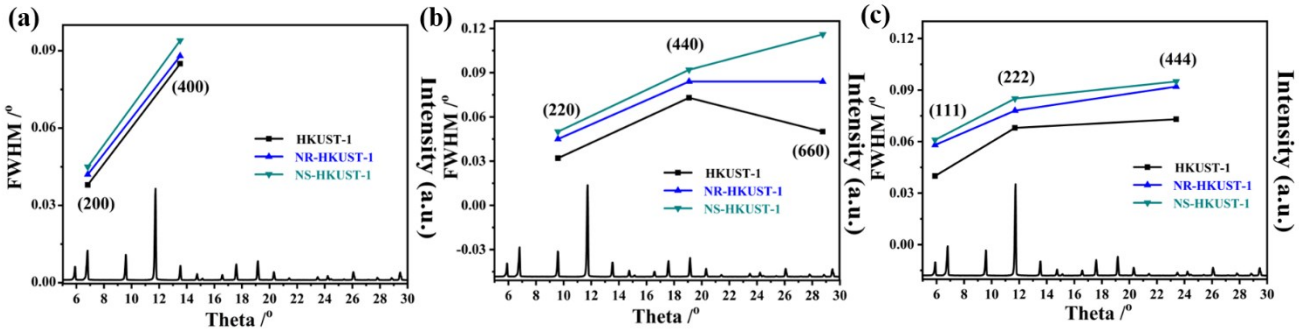


**Fig. S32.** Comparison of FWHM patterns of defective NR-HKUST-1 and NS-HKUST-1 with parent HKUST-1 in a different direction of faces. (a): <100>; (b):<110>; (c):<111>.

## The blank control experiments:

**Table S3.** Reference experiments for catalyst (HKUST-1, NR-HKUST-1 and NS-HKUST-1) under different catalytic conditions (80 mM $Na_2S_2O_8$, 5 mg catalyst and 10 mL 0.1 M NaOH aqueous solution)

| Electron acceptor | Catalyst | Irradiation | OER activity (maximum oxygen evolution (μmol/g)) |
|---|---|---|---|
| $Na_2S_2O_8$ | - | Yes | No |
| - | HKUST-1 | Yes | No |
| - | NR-HKUST-1 | Yes | No |
| - | NS-HKUST-1 | Yes | No |
| $Na_2S_2O_8$ | HKUST-1 | Yes | 16072 |
| $Na_2S_2O_8$ | NR-HKUST-1 | Yes | 28058 |
| $Na_2S_2O_8$ | NS-HKUST-1 | Yes | 22873 |
| $Na_2S_2O_8$ | HKUST-1 | No | 902 |
| $Na_2S_2O_8$ | NR-HKUST-1 | No | 929 |
| $Na_2S_2O_8$ | NS-HKUST-1 | No | 917 |

## Solid-state UV-vis reflectance spectra of planar defect variants and parent HKUST-1:

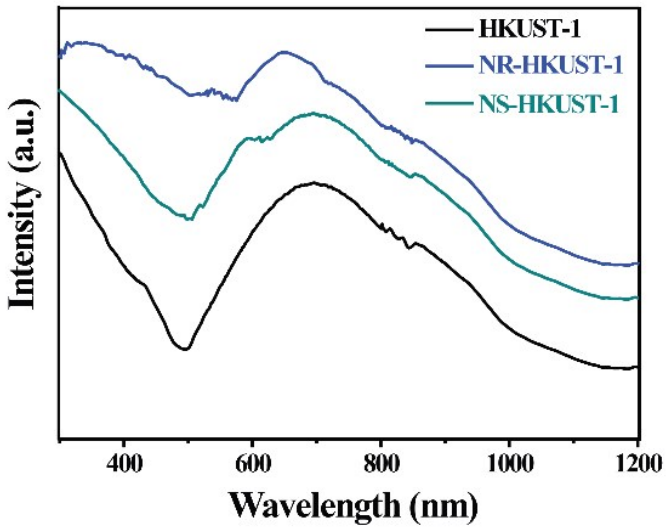


**Fig. S33.** Solid-state UV-vis reflectance spectra of HKUST-1, NR-HKUST-1 and NS-HKUST-1.

### XPS analysis of planar defect variants with different w ($Cu^{1+}/Cu^{2+}$):

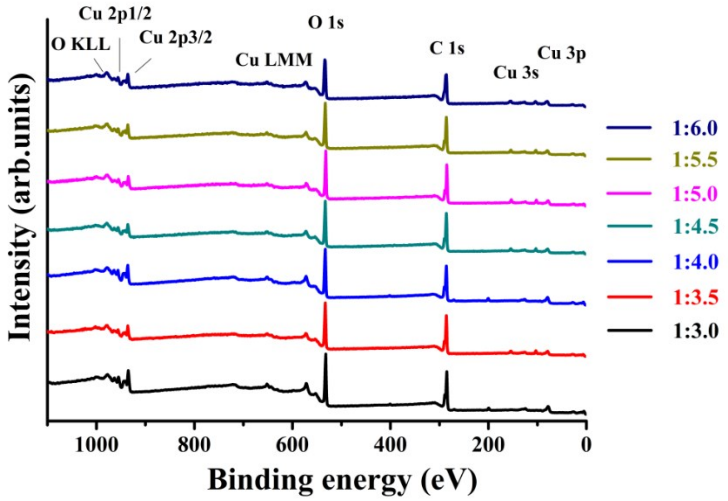


**Fig. S34.** XPS survey scans for planar defect variants with different w ($Cu^{1+}/Cu^{2+}$).

The planar defect variants with different w ($Cu^{1+}/Cu^{2+}$) were further characterized by XPS. The XPS data provide direct spectroscopic evidence for the presence of different content of w ($Cu^{1+}/Cu^{2+}$) achieved by adding different concentrations of vanillin. The XP spectra of all samples show the dominanting peaks characteristic for elements copper, oxygen and carbon (Fig. S34).

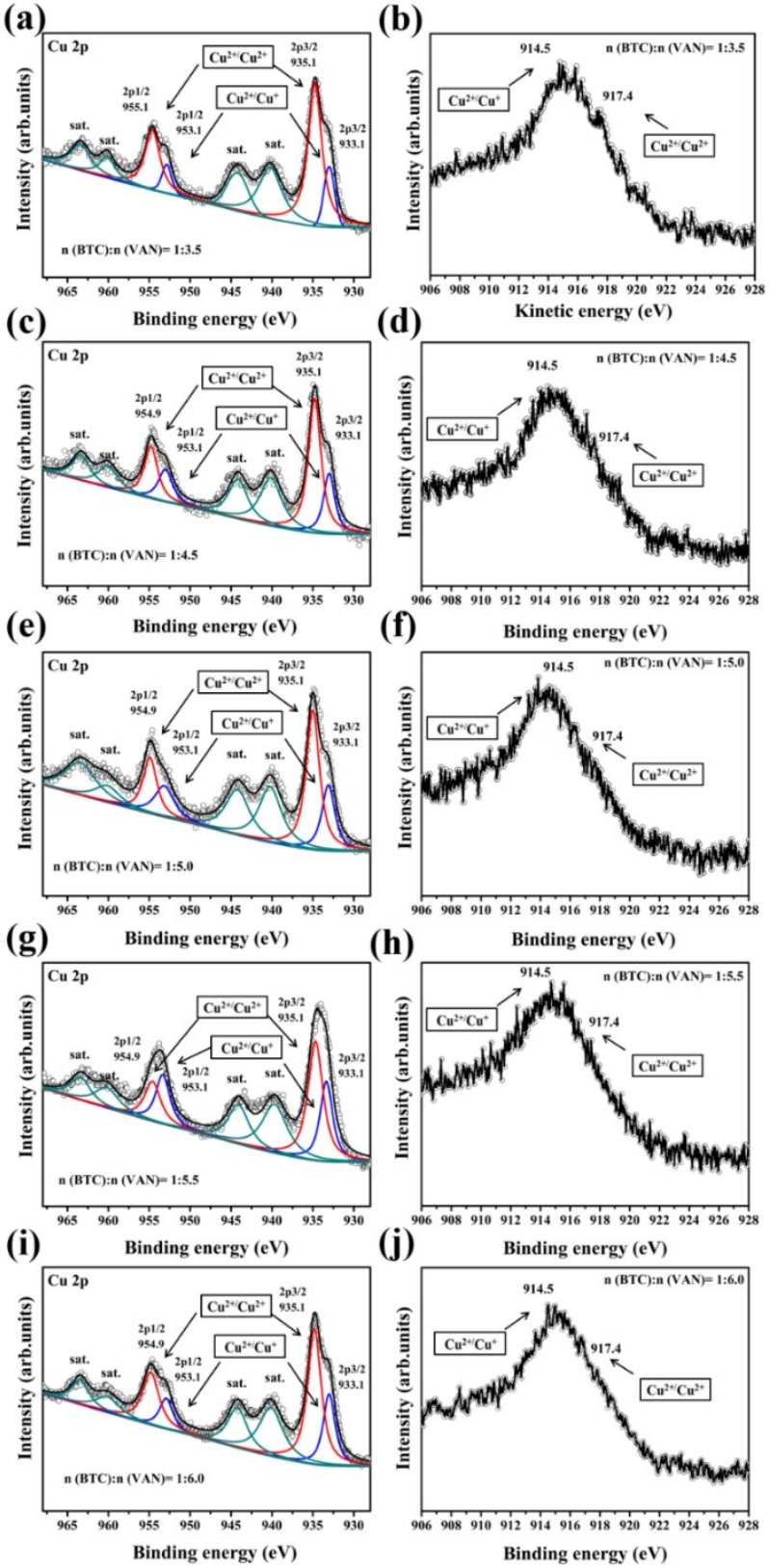


**Fig. S35.** Deconvoluted Cu 2p peaks (a, c, e, g, i) and Auger spectra (b, d, f, h, j) for the planar defect variants with different w ($Cu^{1+}/Cu^{2+}$).

As shown in Fig. S32, For Cu 2p, the analysis is the same as in Figure S16. When n(BTC):n(VAN) is 1:3.5, 1:4.5, 1:5.0, 1:5.5 and 1:6.0, $Cu^{1+}/Cu^{2+}$ dimer of planar defect variants appeared at binding energies of 933.1 and 953.1 eV and the content of w ($Cu^{1+}/Cu^{2+}$) is 19.41%, 23.58%, 32.37%, 35.66%, 41.13% and 41.95%, respectively. The presence of two kinds of dimers was further supported by the Auger peaks at ~914.5 eV for $Cu^{1+}/Cu^{2+}$ and at ~917.3 eV as a shoulder for $Cu^{2+}/Cu^{2+}$ species.

**The comparison blank of others works:**

**Table S4.** Comparison of the catalytic performance and recyclability of our defective HKUST-1 with reported catalysts.

| Catalyst | Reaction condition | Evolved oxygen | Evolved oxygen after 5 cycles | Ref. |
|---|---|---|---|---|
| NR-HKUST-1 variant (n(BTC):n(VAN) = 1:5.5) | 300 W Xe lamp ($\lambda \geq 420$ nm); 5 mg catalyst; 80 mM $Na_2S_2O_8$; 10 mL NaOH aqueous solution (pH = 9); vigorous stirring. | 3784.2 μmol/g/h | 1155.6 μmol/g/h | This work |
| NR-HKUST-1 | 300 W Xe lamp ($\lambda \geq 420$ nm); 5 mg catalyst; 80 mM $Na_2S_2O_8$; 10 mL NaOH aqueous solution (pH = 9); vigorous stirring. | 3117.6 μmol/g/h | - | This work |
| NS-HKUST-1 | 300 W Xe lamp ($\lambda \geq 420$ nm); 5 mg catalyst; 80 mM $Na_2S_2O_8$; 10 mL NaOH aqueous solution (pH = 9); vigorous stirring. | 2541.4 μmol/g/h | 2288.9 μmol/g/h | This work |
| Cu-ZIF-400 | catalyst (0.20 g/L); NaPi buffer solution (pH 7.0, 10.0 mL); $Na_2S_2O_8$ (5.0 mM); $[Ru(bpy)_3]Cl_2$ (1.0 mM); LED lamp, k 420 nm | 53.4 μmol/g/h | 51.2 μmol/g/h | 9 |
| $Pt@Cu_2O/WO_3$ | 0.300 g photocatalyst; 200 mL of 0.01 M aqueous $AgNO_3$ solution; 300 W Xe lamp without cut-off filter | 1238.6 μmol/g/h | 1114.7 μmol/g/h | 10 |

| | | | | |
|---|---|---|---|---|
| $Co@Co_3O_4$ | 5 mg photocatalysts; 80 mM $Na_2S_2O_8$; 10 mL 0.1 M NaOH; 20 mL water; 300 W, Xe lamp, $\lambda > 420$ nm | 2778 μmol/g/h | 2499.0 μmol/g/h | 11 |
| Red $TiO_2$ - $RuO_2$ co-catalyst | 100 mg $TiO_2$ with $RuO_2$ modification was dispersed in 100 mL aqueous solution containing 0.85 g $AgNO_3$; The reaction temperature: 10 °C; 300 W Xe lamp ($\lambda = 420$ nm). | 81.6 μmol/g/h | 17.5 μmol/g/h | 12 |
| $BiO_{2-x}$ UTNSs | 20 mg photocatalysts; 2 mg methyl viologen; 80 mL water; 300 W Xe lamp, AM 1.5 G | 2715.4 μmol/g/h | 1810.3 μmol/g/h | 13 |
| Mo doped $Bi_2WO_6$ | 0.1 g of photocatalysts; 0.1 M NaOH; 0.02 M $Na_2S_2O_8$; 100 mL water; 300 W Xeon lamp, $\lambda > 420$ nm | 147.2 μmol/g/h | - | 14 |
| $BiVO_4$ | 0.5 g photocatalysts; 850 mg $AgNO_3$; 270 mL water; 300 W Xeon lamp, $\lambda > 420$ nm | 492 μmol/g/h | - | 15 |
| g-$C_3N_4$/$BiVO_4$ | 0.02 g photocatalysts; 0.05 M $AgNO_3$; 12 mL water; 300 W Xeon lamp, $\lambda > 420$ nm | 328 μmol/g/h | - | 16 |
| 0.5% FeOOH NSs/$BiVO_4$ | 0.1 g photocatalyst; 0.85 g of $AgNO_3$; 270 mL of water; 300 W Xe lamp ($\lambda > 400$ nm). | 1130.0 μmol/g/h | - | 17 |

## Recycle study and comparison of PXRD, SEM and $N_2$ BET patterns:

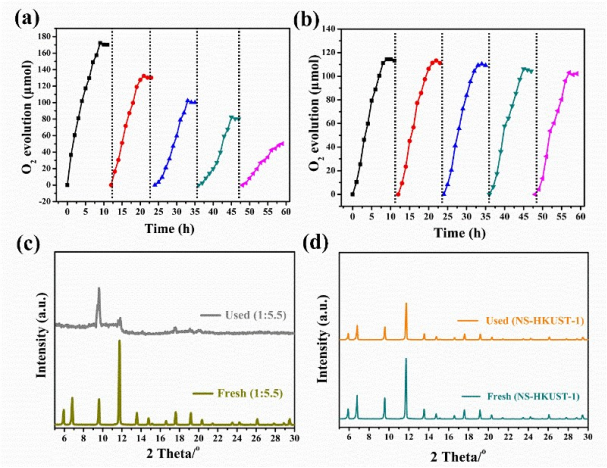


**Fig. S36.** (a) Recycle study of NR-HKUST-1 variant was synthesized (n(BTC):n(VAN) = 1:5.5) in the light-driven water oxidation reaction, the reaction system was evacuated after each run; (b) Recycle study of NS-HKUST-1 in the light-driven water oxidation reaction, the reaction system was evacuated after each run; (c) Comparison of PXRD patterns of fresh NR-HKUST-1 variant was synthesized (n(BTC):n(VAN) = 1:5.5) with recycled variant after 5 cycles; (d) Comparison of PXRD patterns of fresh NS-HKUST-1 with recycled variant after 5 cycles.

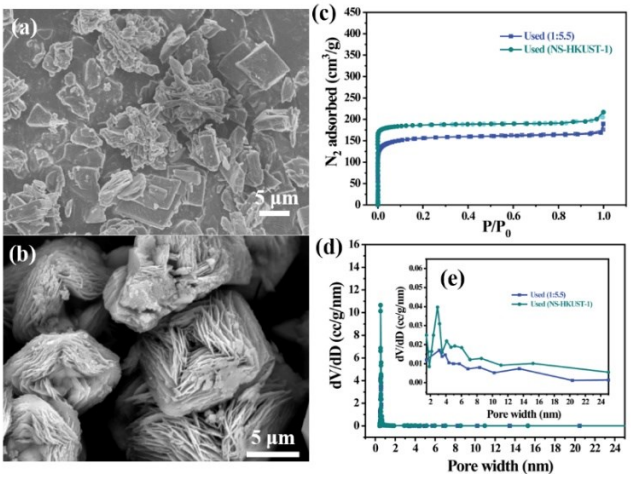


**Fig. S37.** SEM images of NR-HKUST-1 variant (n(BTC):n(VAN) = 1:5.5) (a) and NS-HKUST-1(b) after recycling 5 times, and the $N_2$ adsorption/desorption isotherms (c) and pore size distribution curves (d-e) at 77 K of defective NR-HKUST-1 variant (n(BTC):n(VAN) = 1:5.5) and NS-HKUST-1 after recycling 5 times.

**Table S5** BET surface areas and pore features of defective NR-HKUST-1 variant (n(BTC):n(VAN) = 1:5.5) and NS-HKUST-1 after recycling 5 times.

| Sample | $S_{BET}$[a] ($m^2/g$) | Pore volumes ($cm^3/g$) | | |
|---|---|---|---|---|
| | | $V_{total}$[b] | $V_{micro}$[c] | $V_{meso}$[d] |
| NR-HKUST-1 | 1187 | 0.5442 | 0.5216 | 0.0239 |
| NS-HKUST-1 | 836 | 0.3484 | 0.3267 | 0.0220 |

[a] **SBET**: Brunauer–Emmett–Teller (BET) surface area. [b] **Vtotal**: Total pore volume calculated from the nitrogen adsorption data at $P/P_0 = 0.998$. [c] **Vmicro**: Micropore volume obtained by the t-plot method. [d] **Vmeso**: Mesopore volume calculated by the Barrett–Joyner–Halenda (BJH) adsorption method.

## References


1 B. Sun, S. Kayal, *Energy*, 2014, **76**, 419-427.

2 W.W. Lestari, R.E. Nugraha, I.D. Winarni, M. Adreane, F. Rahmawati, *AIP Conference Proceedings*, 2016, **1725**, 020038.

3 M. Todaro, A. Alessi, L. Sciortino, S. Agnello, M. Cannas, F.M. Gelardi, G. Buscarino, *J. Spectrosc.*, 2016, **2016**, 1-7.

4 Y. Peng, H. Huang, Y. Zhang, C. Kang, S. Chen, L. Song, *Nat. Commun*., 2018, **9**, 187.

5 Z. Fang, J.P. Dürholt, M. Kauer, W. Zhang, C. Lochenie, B. Jee, B. Albada, N. Metzler-Nolte, A. Pöppl, B. Weber, M. Muhler, Y. Wang, R. Schmid, R.A. Fischer, *J. Am. Chem. Soc.*, 2014, **136**, 9627-9636.

6 Z. Wang, L. Ge, M. Li, R. Lin, H. Wang, Z. Zhu, *Chem. Eng. J*., 2019, **357**, 320-327.

7 L. Zhou, Z. Niu, X. Jin, L. Tang, L. Zhu, *ChemistrySelect.*, 2018, **3**, 12865-12870.

8 H. Niu, S. Liu, Y. Cai, F. Wu, X. Zhao, *Micropor. Mesopor. Mat.*, 2016, **219**, 48-53.

9 Y. Zhang, X. Zhou, F. Zhang, T. Tian, Y. Ding, H. Gao, *J. Catal.*, 2017, **352**, 246-255.

10 H. Gong, Y. Zhang, Y. Cao, M. Luo, Z. Feng, W. Yang, K. Liu, H. Cao, H. Yan, *Appl. Catal. B-Environ.*, 2018, **237**, 309-317.

11 B. Sun, Y. Qian, Z. Liang, Y. Guo, Y. Xue, J. Tian, H. Cui, *Mat. Sol. C.*, 2019, **195**, 309-317.

12 X. Hong, J. Tan, H. Zhu, N. Feng, Y. Yang, J.T.S. Irvine, L. Wang, G. Liu, H.-M. Cheng, *Chem. Eur. J.*, 2019, **25**, 1787-1794.

13 D. Wang, J. Guo, D. Hu, Q. Xu, L. Zhang, J. Wang, *ACS. Sustain. Chem. Eng.*, 2018, **6**, 8300-8307.

14 Y. Hu, A. Etogo, R. Liu, J. Ren, L. Qi, C. Zheng, J. Ning, Y. Zhong, *J. Mater. Chem*., 2016, **4**, 13242-13250.

15 Z. Yi, J. Ye, N. Kikugawa, T. Kako, S. Ouyang, H. Stuart-Williams, H. Yang, J. Cao, W. Luo, Z. Li, Y. Liu, R. Withers, *Nat. mater.*, 2010, **9**, 559-564.

16 H.J. Kong, D.H. Won, J. Kim, S. Woo, *Chem. Mater.*, 2016, **28**, 1318-1324.

17 G. Ge, M. Liu, C. Liu, W. Zhou, D. Wang, L. Liu, J. Ye, *J. Mater. Chem. A*, 2019, **7**, 9222-9229.